JGR Oceans

RESEARCH ARTICLE
10.1029/2018JC014688

Modeling Ocean Eddies on Antarctica's Cold Water Continental Shelves and Their Effects on Ice Shelf Basal Melting

Stefanie L. Mack[1], Michael S. Dinniman[2], John M. Klinck[2], Dennis J. McGillicuddy Jr.[3], and Laurence Padman[4]

[1]Applied Physics Laboratory, University of Washington, Seattle, WA, USA, [2]Center for Coastal Physical Oceanography, Old Dominion University, Norfolk, VA, USA, [3]Woods Hole Oceanographic Institution, Falmouth, MA, USA, [4]Earth and Space Research, Seattle, WA, USA

Key Points:
- Eddies on Antarctic cold water continental shelves are seasonally varying and unresolved by typical ocean models
- Eddy characteristics in these regions are sensitive to model grid spacing and smoothness of model topography
- In an eddy permitting model of the Ross Sea, eddies cross the ice shelf front but do not contribute to ice shelf basal melt

Correspondence to:
S. L. Mack,
macksl@uw.edu

Citation:
Mack, S. L., Dinniman, M. S., Klinck, J. M., McGillicuddy, D. J. Jr., & Padman, L. (2019). Modeling ocean eddies on Antarctica's cold water continental shelves and their effects on ice shelf basal melting. *Journal of Geophysical Research: Oceans*, *124*, 5067–5084. https://doi.org/10.1029/2018JC014688

Received 16 OCT 2018
Accepted 27 JUN 2019
Accepted article online 4 JUL 2019
Published online 22 JUL 2019

Abstract Changes in the rate of ocean-driven basal melting of Antarctica's ice shelves can alter the rate at which the grounded ice sheet loses mass and contributes to sea level change. Melt rates depend on the inflow of ocean heat, which occurs through steady circulation and eddy fluxes. Previous studies have demonstrated the importance of eddy fluxes for ice shelves affected by relatively warm intrusions of Circumpolar Deep Water. However, ice shelves on cold water continental shelves primarily melt from dense shelf water near the grounding line and from light surface water at the ice shelf front. Eddy effects on basal melt of these ice shelves have not been studied. We investigate where and when a regional ocean model of the Ross Sea resolves eddies and determine the effect of eddy processes on basal melt. The size of the eddies formed depends on water column stratification and latitude. We use simulations at horizontal grid resolutions of 5 and 1.5 km and, in the 1.5-km model, vary the degree of topography smoothing. The higher-resolution models generate about 2–2.5 times as many eddies as the low-resolution model. In all simulations, eddies cross the ice shelf front in both directions. However, there is no significant change in basal melt between low- and high-resolution simulations. We conclude that higher-resolution models (<1 km) are required to better represent eddies in the Ross Sea but hypothesize that basal melt of the Ross Ice Shelf is relatively insensitive to our ability to fully resolve the eddy field.

1. Introduction

Ocean-driven melting of Antarctic ice shelves can affect the future stability of the Antarctic Ice Sheet (Mercer, 1978) and is a large uncertainty when predicting sea level rise (Nowicki et al., 2013). Basal melting around Antarctica makes up over half of ice shelf mass loss, with the remainder being through iceberg calving (Depoorter et al., 2013; Rignot et al., 2013). If melting exceeds the mass inputs to the ice shelf from ice flow across the grounding line and snowfall, the reduction in ice shelf mass reduces the "buttressing" effect—the ability of an ice shelf to hold back and slow the flow of ice (Dupont & Alley, 2005; Goldberg et al., 2009). An ice shelf undergoing rapid thinning by excess basal melting, such as Pine Island Glacier at present (Dutrieux et al., 2014; Jacobs et al., 2011; Pritchard et al., 2012), may become an outlet through which the Antarctic Ice Sheet drains and contributes to sea level rise.

Basal melt occurs in three main modes, defined by the process causing the melting (Jacobs et al., 1992). Mode 1 melt is driven by dense and salty shelf waters that are at or near the surface freezing point ($\approx -1.9\,^{\circ}C$) on the continental shelf and cause melting near the grounding line due to the depression of the freezing point of water with pressure. Mode 2 melt is driven by subsurface waters, originating off the continental shelf, that are significantly above freezing, mainly Circumpolar Deep Water (CDW; $\approx 1\,^{\circ}C$) and modified CDW. Mode 3 melt occurs along the ice shelf front where seasonally warmed surface waters are advected under the ice shelf. The relative importance of melting modes varies from one ice shelf to another: large cold water shelves, such as the Ross, Filchner-Ronne, Amery, and Larsen C, are dominated by Modes 1 and 3 (e.g., Joughin & Padman, 2003). Mode 2 dominates most ice shelves in the Amundsen and Bellingshausen Seas.

The most rapid ice shelf thinning occurs where Mode 2 melt dominates (Pritchard et al., 2012). Recent observations have demonstrated that eddy processes are necessary to transport warm CDW onto the continental shelf where it can enter the ice shelf cavity (Couto et al., 2017; Martinson & McKee, 2012; Moffat

et al., 2009). Idealized models (Stewart & Thompson, 2015) confirm these observations and show that eddies are necessary to represent the interaction between a Rossby wave along the shelf break and a bathymetric trough, leading to trough-induced intrusions of CDW (St-Laurent et al., 2013). A series of realistic ocean models illustrate the importance of eddy-mediated heat transfer onto the continental shelf in East Antarctica (Hattermann et al., 2014), the Amundsen Sea (Nakayama et al., 2014; St-Laurent et al., 2015), the west Antarctic Peninsula (Graham et al., 2016), and Prydz Bay (Liu et al., 2017). A comprehensive modeling study of on-shelf heat transport around Antarctica found that eddies drive the net shoreward heat transport onto the continental shelves (Stewart et al., 2018).

Few prior studies have investigated the effects of eddy-mediated heat fluxes on cold water Antarctic continental shelves and under their ice shelves. Eddy-resolving models are computationally expensive: to resolve the eddy transport of CDW onto the continental shelf, horizontal grid spacings of less than 2 km are required (Graham et al., 2016; Hattermann et al., 2014; Liu et al., 2017; St-Laurent et al., 2015). For the weaker stratification of cold water regions and near the ice shelf front, even finer grids are needed; for example, Årthun et al. (2013) found that a subkilometer horizontal grid was necessary to study the eddy transport of heat across the ice front in an idealized domain. These analyses suggest that quantifying eddy effects on the stability of the large cold water ice shelves, where Mode 1 and Mode 3 dominate, requires high-resolution grids. Alternatively, improved parameterizations of the eddy contribution to net heat fluxes could be developed for these conditions.

Before taking on the significant computational expense of regional ocean models run at subkilometer horizontal grid spacing, we investigate the complexity inherent in modeling eddies in Antarctic cold water continental shelf seas. Eddies exist at a continuum of sizes, and their size at formation is dependent on the ocean state including stratification (see section 2). Eddies formed at different locations on an Antarctic continental shelf may be different sizes, and processes such as deep winter convective mixing erase stratification so that a model's ability to resolve eddies depends not only on location but also on season.

We use a regional ocean model of the Ross Sea as a test case for determining the importance of eddies on an Antarctic cold water continental shelf. During the winter, deep convective mixing events north of the ice front greatly reduce the stratification, which increases again in spring and summer as the surface is warmed and sea ice melts. These changes in stratification provide a strong seasonality to a model's ability to resolve small-scale ocean structure.

The paper is structured as follows. A brief overview of eddy theory (section 2) sets what we expect in the Ross Sea. We then describe the regional ocean model and detail a series of calculations, including the partition of kinetic energy (KE) into its components, an eddy tracking algorithm, and how we separate Mode 1 and Mode 3 basal melt (section 3). In section 4 we identify where the model is and is not eddy resolving, describe the dependence of the components of KE on model characteristics and season, and track the location and characteristics of eddies in the simulations. We finish with an analysis of the simulated eddy effect on Mode 1 and Mode 3 basal melt. Section 5 synthesizes and discusses the results.

2. Eddy Theoretical Overview

We define several common terms in the context of this study. The Rossby radius of deformation (a) indicates the horizontal scale at which rotation effects are as important as buoyancy effects

$$a = \frac{c}{|f|}. \tag{1}$$

Here, f is the Coriolis frequency and c is the gravity wave speed. For the barotropic case, c is the surface gravity wave speed. For baroclinic applications in a stratified water column, c depends on the baroclinic mode number (m) and the vertical structure of the buoyancy frequency $N(z)$ and is estimated following Chelton et al. (1998):

$$c_m = \frac{1}{m\pi} \int_{-H}^{0} N(z)\mathrm{d}z, \tag{2}$$

where H is the total water column depth. For the remainder of this paper, we focus on the first ($m = 1$) baroclinic mode (Rossby radius = a_1).

We also specify the spatial scale referred to as the "mesoscale." Dynamically, the mesoscale is the horizontal scale at which the flow is quasi-geostrophic, turbulence is two dimensional, and nonhydrostatic effects are small. Following McWilliams (2008), mesoscale eddy flows have small aspect ratios, among other criteria. We set a lower limit on the mesoscale using the aspect ratio of water depth over horizontal length scale. For the Ross Sea, with typical on-shelf depths of 500 m, the length scale should be an order of magnitude higher, around 5 km. We therefore describe submesoscale eddies as eddies where $a_1 \leq 5$ km. The upper limit of the mesoscale is not precisely defined. Nondynamically, the mesoscale refers to processes smaller than basin scale: a reasonable upper limit to the mesoscale is an order of magnitude below the width of the continental shelf or around 100 km. On the Ross Sea continental shelf, with a characteristic depth of 500 m at around 75°S, the barotropic Rossby radius ($a_0 \sim 500$ km) is larger than the mesoscale upper limit. Note that a more common and formal definition of mesoscale is the horizontal scale of motion similar to the first radius of deformation (as in Su et al., 2014, 2016). We avoid using this definition here, as a_1 is precisely what we are investigating.

2.1. Eddy Scales

Several classic baroclinic instability problems examine the initiation and evolution of eddies formed under idealized circumstances. In general, in the strongly unstable limit, the horizontal scale at which eddies form and their approximate lifetime can be predicted as functions of the mean state (Smith & Vallis, 2002). Eddy radius at formation is proportional to a_1. In the Eady problem (Eady, 1949), the most unstable wavelength is 4 times a_1, while in the Charney problem (Charney, 1947), it is the same as a_1. Satellite observations confirm this scale, showing a KE source near a_1 (Scott & Wang, 2005) and an ocean eddy radius approximately 2–5 times larger than the wavelength of the most unstable waves (Stammer, 1998).

After formation, eddy radius is determined in part by the energy cascade. Ocean energy is transferred from large scales to smaller scales through nonlinear turbulent interactions and dissipates through the breaking of internal waves and through friction at the seafloor, under ice shelves, and under sea ice when internal stresses prevent free ice drift. This transfer maintains an approximate long-term balance with energy input from winds, surface buoyancy fluxes, and tides. Energy in mesoscale ocean eddies can also move in an inverse cascade, from high mode baroclinic eddies to low mode baroclinic eddies and then to barotropic eddies (Ferrari & Wunsch, 2009). The transfer to a lower mode occurs when a baroclinic eddy reaches a_m for its current mode m (Charney, 1971). Nonuniform stratification interferes with this process, causing the transfer of energy between modes to be less direct and efficient and leaving the energy concentrated around a_m (Smith & Vallis, 2001). This theory does not take into account interactions with topography and the presence of large-scale potential vorticity gradients (such as near an ice shelf front) that can modify the energy cascade (McWilliams, 2008). Generally, the size of an eddy after formation is affected by nearby energy sources and sinks, including other eddies, and the direction of the energy cascade.

Time scales of eddy duration can be estimated for a steady-state system, where energy put into eddies is replenished in the mean flow, and eddies do not travel to another region, that is, there are no nonlocal effects. With these assumptions, time scales are proportional to the ratio of a_m and the mean flow speed (see ; Vallis, 2006, for a comprehensive overview of instability problems and associated scales). Global observations of eddies (Chelton et al., 2007) show eddy durations of weeks to months, with a few exceptions.

After formation, eddies in the Ross Sea can change size based on the direction of the energy cascade. Eddies that move away from their formation region to areas without energy sources will lose energy to friction and internal mixing and break apart. Eddies that have access to an energy source, such as horizontal density gradients, mean flow KE, tidal energy (not included in these simulations), or energy from other eddies experience the inverse energy cascade and grow, potentially transitioning from Mode 1 baroclinic to barotropic.

Interactions with topography also can have a substantial impact on individual eddies. Gille et al. (2000) found that, in the ACC, eddy kinetic energy (EKE) was correlated with seafloor roughness at depths less than 3,000 m but anticorrelated at depths greater than 4,800 m. Rough topography can produce variability in flow, creating instabilities or density gradients that fuel eddies, and is also an energy dissipation mechanism. In the Ross Sea, notable topographic features include the shelf break, several large banks on the continental shelf, and the ice shelf front. The shelf break and ice shelf front act as potential vorticity barriers to eddies, although eddies can cross either barrier by following constant f/H contours (ratio of Coriolis parameter to water column depth) (Grosfeld et al., 1997; Li et al., 2017).

Based on geostrophic turbulence theory and the physical geometry of the Ross Sea, we can summarize expected eddy behavior in the Ross Sea. Mesoscale eddies would form as Mode 1 baroclinic eddies. Barotropic eddies are too large to form on the continental shelf, and higher mode baroclinic eddies would be small and classified as submesoscale. The weak stratification (small a_1) over much of the Ross Sea indicates that there is not much potential energy available to sustain or grow eddies, particularly if they leave the area of formation.

3. Methods

3.1. Regional Ocean Modeling

Our Ross Sea model (see Figure 1) uses the Regional Ocean Modeling System (ROMS v3.6) with finite differencing schemes and terrain-following vertical levels (sigma coordinate system; Haidvogel et al., 2008; Shchepetkin & McWilliams, 2005, 2009). The configuration used here is similar to Mack et al. (2017; without tidal forcing) except that the bottom mixed layer parameterization is turned off, which is a modification from the version reported by McGillicuddy et al. (2015) and Dinniman et al. (2007, 2011). The Ross Ice Shelf is included as a floating static ice shelf, with parameterizations for thermodynamic and mechanical interactions with the water underneath (Dinniman et al., 2011). Heat and salt fluxes between the ocean and ice base are parameterized using heat and salt transfer coefficients that are functions of the friction velocity (Holland & Jenkins, 1999); see section 3.4 for more details. The ocean model is coupled to a dynamic sea ice model (Budgell, 2005). The vertical coordinate system follows Song and Haidvogel (1994). We use 24 vertical levels that are concentrated near the surface (ocean surface or ice shelf base) and the sea floor.

For the advection of momentum and tracers, we used a third-order upwind scheme in the horizontal and fourth-order centered in the vertical. Lateral diffusivity is 5 m^2/s and lateral viscosity is 0.1 m^2/s (as in Dinniman et al., 2011), where lateral mixing occurs along model layers for momentum and along geopotential surfaces for tracers. Vertical mixing of tracers and momentum is determined with the KPP scheme (Large et al., 1994). ROMS does not include a parameterization of thermobaric convection, which may influence the eddy field (e.g., Su et al., 2016).

Simulations were run at horizontal grid spacings of 5 and 1.5 km. To resolve eddies, the grid spacing needs to be at least a factor of 2 smaller than a_1 (Hallberg, 2013). The typical value of a_1 for Antarctic continental shelves is estimated to be around 5 km (Hallberg, 2013), which is also the lower limit for our operational definition of the mesoscale. For this value of a_1, the 1.5-km horizontal grid would be eddy resolving, while the 5-km grid would not, although the latter may be eddy permitting.

Following a 6-year spin-up, simulations were run for the period 15 September 2010 to 27 February 2012. Forcing includes ERA-Interim winds and atmospheric temperatures every 6 hr and monthly climatologies of humidity, precipitation, and cloud cover (Dee et al., 2011), interpolated from the original 80-km product to the model grid. At the open boundaries, sea ice concentration is set from monthly SSM/I data, ocean temperatures, and salinities are from World Ocean Atlas 2001 monthly climatology, and barotropic velocities are from Ocean Circulation and Climate Advanced Model (Webb et al., 1997). Our model does not include tidal forcing.

Model bathymetry was interpolated from gridded observational-based products onto our grid: BEDMAP2 (Fretwell et al., 2013) for the ice shelf and cavity topography and IBCSO (Arndt et al., 2013) for ocean bathymetry outside of the ice shelf cavity. The sigma coordinate system of ROMS requires changes in bathymetry between grid points to be small with respect to total water column depth and changes in sigma layer position to be small relative to the local layer thickness to avoid pressure gradient errors. We smoothed the bathymetry and ice draft to reasonable values of the Beckmann and Haidvogel number (commonly known as rx0; Beckmann & Haidvogel, 1993) and the Haney number (rx1; Haney, 1991) . A short test simulation with horizontally uniform and vertically varying stable stratification confirmed that, after grid smoothing, no significant velocities were generated from grid-induced pressure gradient errors.

Generating the model geometry for the 1.5-km grid could be accomplished in two ways: (1) interpolation from gridded observational based data followed by smoothing for rx0 and rx1, giving a "rougher" bathymetry and (2) interpolation from the 5-km grid, which requires no additional smoothing and has relatively "smoother" bathymetry (Figure 1). The advantages to option (1) are that more detail is retained from

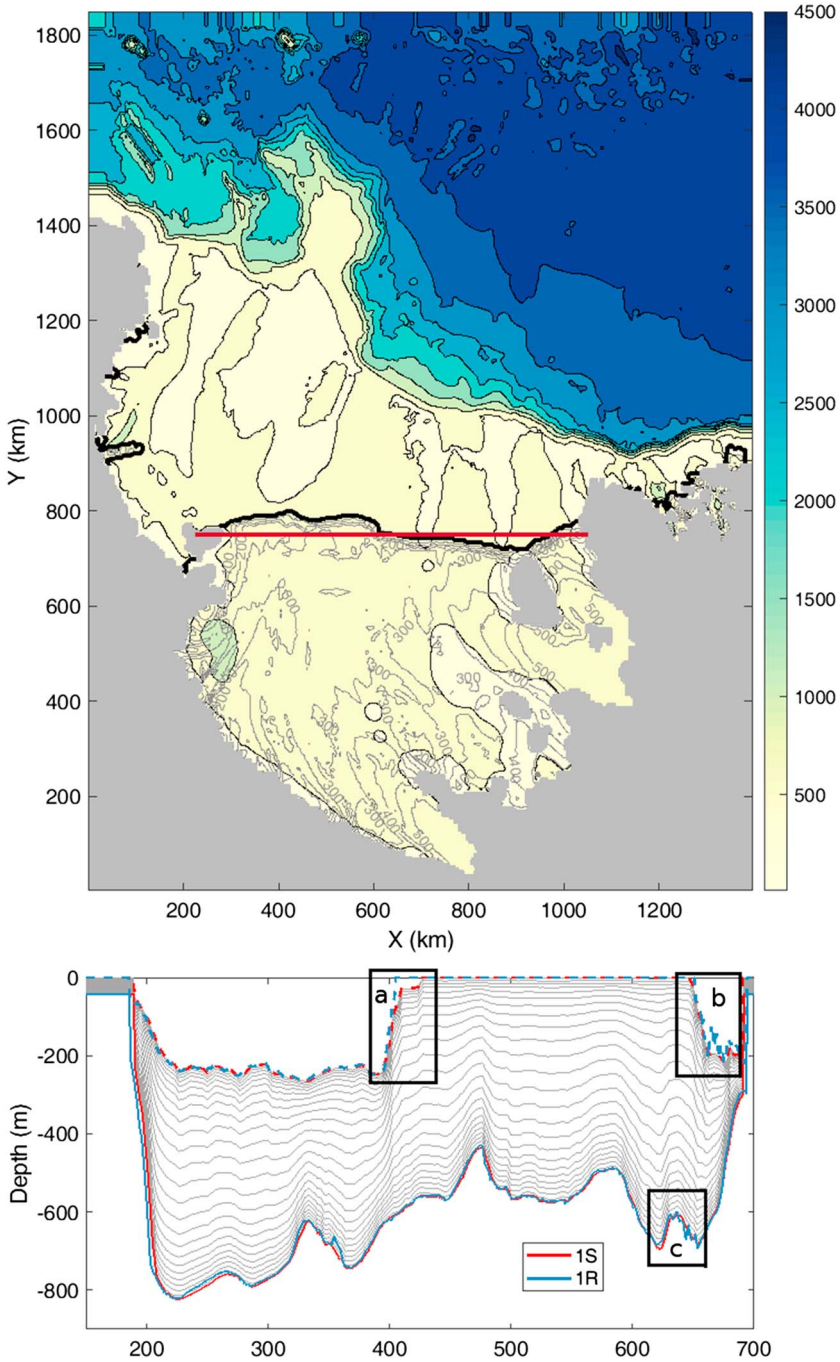

Figure 1. (top) Ross Sea model domain. Bathymetry is from simulation *1S*. Color bar and black contours outline ocean bathymetry; gray contours and labels are ice shelf draft. Gray background is land and grounded ice sheet. Bold black line is the ice shelf front. Red line is the transect shown below. (bottom) Transect of model topography across grid line $y = 500$ for grid *1R* (blue) and *1S* (red). Solid colored lines are ocean bathymetry; dotted lines are ice shelf topography. Thin gray lines are model layers. Boxes indicate areas where the topography is different for the two geometries: (a) ice shelf front is less steep in *1S*, (b) ice shelf topography is "rougher" in *1R*, and (c) ocean bathymetry is "smoother" in *1S*.

observational data sets and the higher-resolution grid permits steeper topographic slopes. However, option (2) is more consistent with the bathymetry details present in the 5-km grid. We chose to proceed with both to disentangle the effects of grid spacing and topographic smoothness, giving three simulations:

- *5*. The 5-km grid interpolated from gridded observational-based data.
- *1R* ("rough"). The 1.5-km grid directly interpolated from data. Topography is rougher, with steeper slopes, due to a finer sampling of bathymetry and ice shelf draft grids.
- *1S* ("smooth"). The 1.5-km grid interpolated from *5*. Topography is the same as *5* and does not contain the finer detail and steeper slopes of *1R*.

3.2. KE

The total mechanical energy in a given ocean volume is the sum of KE and potential energy. Changes to the total energy over time are caused by energy flux divergence through the boundaries of the volume or by internal energy dissipation. Calculating a total energy budget using simulation output is a nontrivial task (MacCready & Giddings, 2016), as energy and volume are not necessarily conserved in the discretized governing equations and are subject to machine precision and round off. For the purposes of this study, we focused on the distribution of KE in both baroclinic and barotropic states and in the time-mean and eddying component.

The standard formulation of KE at any grid cell in a four-dimensional model is written as

$$KE(x, y, z, t) = \frac{1}{2}\boldsymbol{u}(x, y, z, t) \cdot \boldsymbol{u}(x, y, z, t), \tag{3}$$

where $u(x, y, z, t)$ is the three-dimensional velocity vector. We decomposed u into a depth-mean and a depth-varying velocity, which we refer to as barotropic and baroclinic velocities

$$\boldsymbol{u}(x, y, z, t) = \langle \boldsymbol{u} \rangle (x, y, t) + \boldsymbol{u}_z(x, y, z, t). \tag{4}$$

Here, $\langle\rangle$ indicates a mean in the z direction, while subscript z indicates residuals from the depth mean. Decomposing velocity in this fashion defines the separation of baroclinic and barotropic KE. The barotropic and baroclinic velocities are each then decomposed into time-mean and time-varying components to separate eddying flows from the mean flow. Using the barotropic velocity as an example,

$$\langle \boldsymbol{u} \rangle (x, y, t) = \overline{\langle \boldsymbol{u} \rangle}(x, y) + \langle \boldsymbol{u} \rangle'(x, y, t), \tag{5}$$

where the overbar represents a temporal (e.g., monthly) mean and $'$ represents time-varying velocity. The total velocity is then

$$\boldsymbol{u}(x, y, z, t) = \overline{\langle \boldsymbol{u} \rangle}(x, y) + \langle \boldsymbol{u} \rangle'(x, y, t) + \overline{\boldsymbol{u}_z}(x, y, z) + \boldsymbol{u}'_z(x, y, z, t). \tag{6}$$

From this, KE can be rewritten as a series of five terms

$$KE = \overline{KE_{BT}}(x, y) + EKE_{BT}(x, y, t) + \overline{KE_{BC}}(x, y, z) + EKE_{BC}(x, y, z, t) + KE_R, \tag{7}$$

where *BT* indicates barotropic, *BC* indicates baroclinic, and time-varying KE is referred to as eddy kinetic energy (*EKE*). The first four terms on the right-hand side of equation (7) are the calculated KE from the corresponding velocity component. The fifth term, the "residual" term, includes the remaining terms when equation (6) is applied to equation (3). A similar decomposition of KE into specific parts was done by Chen et al. (2016).

All the KE terms are calculated for each individual grid box and then averaged per unit volume

$$\frac{1}{V}\sum KE\Delta V, \tag{8}$$

where $\Delta V = \Delta x \Delta y \Delta z$ is the volume of each grid box and V is the total volume of the domain for which the average is calculated.

3.3. Eddy Tracking

The "eddy" field that is quantified by the EKE terms in the above equations includes a variety of features including the ocean's direct response to weather band changes in wind stress and air temperature, instabil-

ities, and coherent eddies. In this section we describe our approach to determining each simulation's ability to represent coherent eddies.

We estimated eddy activity by directly counting individual eddies in a simulation. There is no universal standard used to define what constitutes an eddy, although there are several often-used methods based on sea surface height (SSH), vorticity, or a combination of both (i.e., the Okubo-Weiss parameter; Chelton et al., 2007; Isern-Fontanet et al., 2003). For this study we used a Matlab function designed to track eddies by SSH (Gaube & McGillicuddy, 2017), which was modified to work with simulation output in x-y coordinates instead of latitude-longitude. A limitation of using SSH criteria as opposed to relative vorticity is that the eddy analysis is restricted to eddies that have some ocean surface height signal. Deep baroclinic eddies may not be identified or tracked using this method. However, we avoid misidentifying other vorticity features, such as the large potential vorticity gradient at the ice shelf front, as eddies. To define an eddy, we impose a set of criteria.

1. The eddy must persist for at least four consecutive days.
2. The maximum SSH of the eddy must be at least 1 cm different from the background.
3. There must be at least 21 grid points contained within an eddy. This corresponds to 5 points across the diameter of the eddy in two orthogonal horizontal directions.
4. The maximum diameter of the eddy is 70 km. This includes most mesoscale eddies but filters out larger eddies.
5. The maximum distance the eddy can travel in 1 day is 100 km. This corresponds to a propagation speed of slightly over 1 m/s, which is an approximate upper bound for velocity in the Ross Sea. It is unlikely that eddies will travel this fast.

These criteria ensure that the features identified by the eddy tracking software actually are eddies and that each eddy track corresponds to only one eddy. Eddies under the ice shelf are also tracked, as SSH is given based on pressure relative to a reference ice shelf draft that is in hydrostatic equilibrium (see; Dinniman et al., 2016, for more details). Once an eddy is identified, it is tracked through the daily instantaneous SSH fields that are output from each simulation, and statistics for individual eddies are recorded, including age, radius, amplitude of SSH, and start day.

One limitation of this method is that we isolate coherent eddies from the full eddy field, ignoring filaments and fronts. Previous studies (e.g., Abernathey & Haller, 2018) have demonstrated that tracer transport is significantly affected by the full turbulent field, not just advective transport by individual coherent eddies. In this study, we use EKE to examine all eddy variability and coherent eddy tracking to characterize a given simulation's ability to allow coherent eddies to appear.

3.4. Ice Shelf Basal Melt

Ice shelf basal melt rate, w_b, for the Ross Ice Shelf in the ROMS model configuration was calculated for grid cells under the ice shelf following the three equation parameterization from Holland and Jenkins (1999)

$$w_b = \frac{-\phi_q}{\rho_i(L_f - c_i\Delta T)}\rho_w c_w, \tag{9}$$

where ϕ_q is the surface heat flux into the ocean computed by the model and ΔT (always ≥ 0) is the temperature difference between the atmosphere and the freezing temperature of seawater, T_f. The model uses $T_{f0} = -1.95$ as a standard freezing temperature for this calculation. The ΔT term accounts for a reduction in heat available for basal melting due to the conductive heat loss through the ice shelf that is related to the temperature gradient between the upper and lower ice surfaces (Holland & Jenkins, 1999). Parameter definitions and values are given in Table 1. Basal melt rates were computed for each model grid cell touching the ice shelf. As the ice shelf is assumed static, w_b does not influence the model geometry. Instead, the effect of ice melting or freezing is parameterized as a salt and heat flux into the top ocean model layer.

The melt rate calculated from equation (9) is dependent on the choice of parameter values in Table 1, which we hold constant in this study and on the heat flux between the ocean and ice shelf base. The heat flux, in turn, depends on the heat content of water that is advected into proximity to the ice base and the processes setting the flux of heat from the ocean to the ice. This flux is evaluated from the temperature differential between the ocean and ice shelf and the turbulence (represented by friction velocity $u*$) at the ice water interface; see section 3 in Holland and Jenkins (1999). In ROMS, $u*$ is evaluated from the quadratic

Table 1
Parameters Used to Calculate Ice Shelf Basal Melt Rates in ROMS

Parameter name	Symbol	Value
Density of ice	ρ_i	930 kg/m^3
Density of water	ρ_w	1,025 kg/m^3
Latent heat of freezing	L_f	3.34×10^5 J/kg
Specific heat of water	c_w	4,000 J·kg^{-1}·K^{-1}
Specific heat of ice	c_i	2,000 J·kg^{-1}·K^{-1}
Temperature of freezing	T_{f0}	−1.95 °C

Note. ROMS = Regional Ocean Modeling System.

stress law using the ice relative velocity of the upper model layer and a specified drag coefficient. The total heat flux is, therefore, influenced by processes affecting ocean circulation, such as wind-driven Ekman pumping setting the mean overturning circulation (e.g., Su et al., 2014; Stewart et al., 2018), velocities from buoyancy-driven meltwater flows, and tides. Here, we focus specifically on the contribution eddies have on the heat flux, by examining changes in basal melt rate at different grid resolutions.

Each ice shelf grid cell was determined to be experiencing Mode 1 melt, Mode 3 melt, or no melt (includes freezing) at each time step. We classified cells as Mode 1 if the temperature of the ocean cell directly under the ice shelf was colder than the surface temperature of freezing for the modeled salinity ($T_f(S, P = 0)$) and as Mode 3 if it was warmer than $T_f(S, P = 0)$. No melt cells are those with a melt rate less than or equal to 0. There is a small amount of Mode 2 melt from CDW, and by this definition, it is included in the Mode 3 melt term. If we chose to distinguish between Mode 1 and Mode 3 with an ice shelf depth criteria (i.e., Mode 3 melt is constrained to parts of the ice shelf that are reachable by Antarctic Surface Water and tend to be the shallower portions of the ice shelf), we get similar values using a depth of 200 m as the cutoff. The thickness of some of the ice along the Ross Ice Shelf front in our simulations is less than 200 m thick as a result of topographic smoothing to satisfy numerical stability criteria.

The mean ice shelf melt rate for the Ross Ice Shelf was calculated as an area and time average and given as a melt rate (w_b) in centimeter per year. Mode 1 and Mode 3 melt were calculated as area sums and averaged over 1 year to produce area-integrated basal mass balance (M_b) values with units of gigatons per year.

4. Results

4.1. Radius of Deformation

We estimated the expected eddy characteristics and behavior from the generalized theory presented in section 2 and the physical characteristics of the Ross Sea. We consider the Ross Sea continental shelf to have two main states: a mostly barotropic state that dominates when deep mixing is stimulated by sea ice formation and brine rejection or strong wind forcing in low sea ice conditions and a mostly baroclinic state when the water column restratifies from surface insolation and sea ice melting in summer.

The radius of deformation (a_1, equation (1)), which determines the horizontal scale of eddy formation, was calculated for the first baroclinic mode using the Gibbs Seawater Toolbox (McDougall & Barker, 2011) to calculate N and equation (2) with $m = 1$ to estimate the internal wave speed. Output from simulation *5* was used to obtain density profiles for calculating N for August (well-mixed) and February (stratified) conditions to determine how a_1 varies spatially and seasonally (Figure 2). Spatially, there are two distinct regions with differing values of a_1: off-shelf and on-shelf including the ice shelf cavity. These regions appear in a histogram as a bimodal distribution (Figure 2 insets), where the mean of each approximately corresponds with one of the peaks (compare with Table 2). In general, a_1 is smaller in August than in February for the entire model domain and when the on-shelf and off-shelf regions are considered separately (Table 2). Based on the histograms in Figure 2, we would need a grid spacing of 350 m or less to capture 95% of the distribution, which is not computationally feasible at this time.

The expected eddy radius at formation, given a potential eddy scale four times a_1, is between 0 and 40 km, the latter being for locations off the continental shelf in February where maximum a_1 is about 10 km (Figure 2b). A substantial portion of the model domain (mostly on-shelf and under the ice shelf) is still not

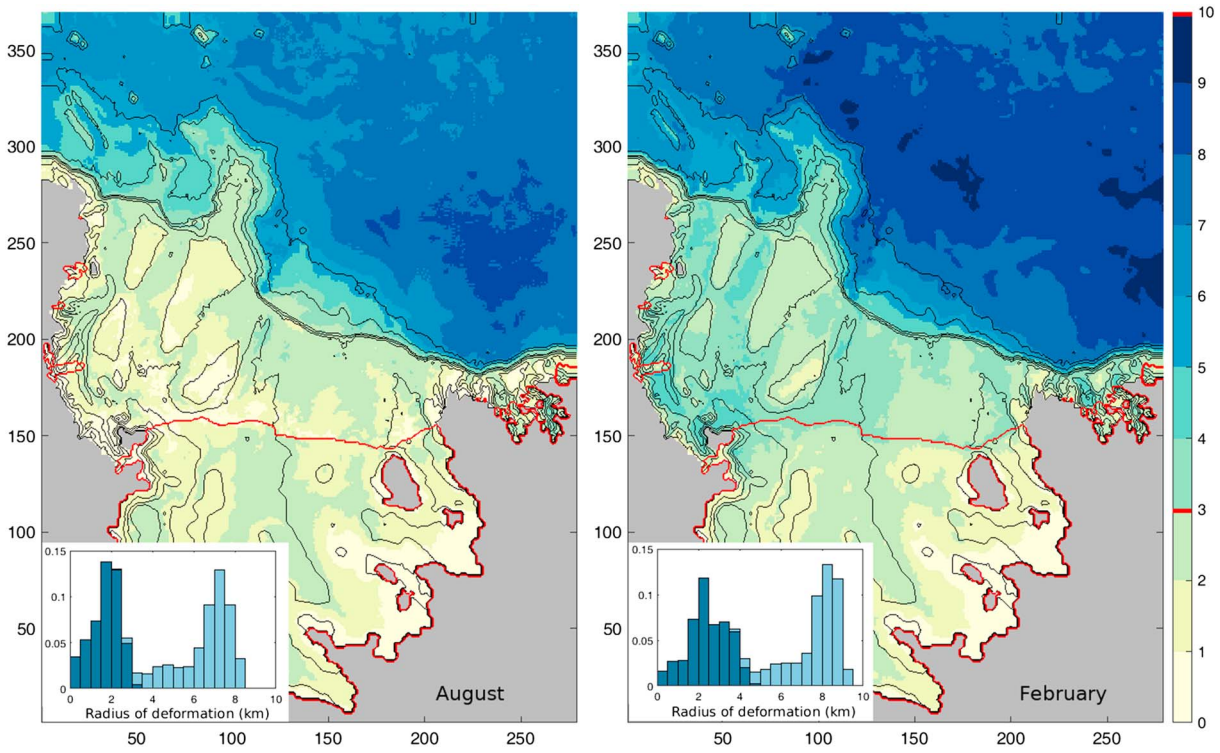

Figure 2. Radius of deformation (a_1, km) calculated from simulation *5*. Inset shows histogram of values over model domain; darker bars indicate the region shoreward of the 700-m isobath. (left) 15 August 2011. (right) 15 February 2012. Red lines on map outline ice shelves. Red lines on color bar indicate minimum radius resolved by the 1.5-km grid (3 km) and by the 5-km grid (10 km).

eddy -resolving: 48% in August, 33% in February for simulations *1R* and *1S*, and 100% in both August and February for simulation *5*. Weak stratification in the water column restricts the transfer of potential energy to EKE when instabilities form. Based on our aspect ratio definition of the mesoscale, eddies with radius less than 5 km fall into the submesoscale regime, where turbulence is no longer quasi-2-D and vertical motion plays a significant role. Submesoscale features are not fully represented in the community version of ROMS, as the model is hydrostatic (Marshall et al., 1997; Marques & Özgökmen, 2014).

4.2. KE Partition

The average barotropic (depth-averaged) velocity fields for August (winter) and February (summer) for simulation *5* (Figure 3) display similar features. August has faster flow along the ice shelf front and far southward under the western side of the ice shelf. In February, this strong barotropic flow under the ice shelf is substantially weaker. Jendersie et al. (2018) found a similar seasonality of the flow under the western ice shelf and attributed it to stronger horizontal density gradients driven by winter sea ice formation. North of the ice shelf, the shelf break jet (the Antarctic Slope Current) and intrusions onto the continental shelf are intensified.

Table 2
Radius of Deformation

Month	Region	Min	Max	Mean	Std	% Not resolved
August	All	0.0 km	8.4 km	4.2 km	2.6 km	*5*: 100%
	On-shelf	0.0 km	4.1 km	1.7 km	0.69 km	*1S*: 48%
	Off-shelf	2.1 km	8.4 km	6.5 km	1.3 km	*1R*: 48%
February	All	0.0 km	9.4 km	5.2 km	2.8 km	*5*: 100%
	On-shelf	0.0 km	5.1 km	2.5 km	0.97 km	*1S*: 33%
	Off-shelf	3.1 km	9.4 km	7.7 km	1.2 km	*1R*: 33%

Note. Given as minimum, maximum, mean, and standard deviation. Corresponds with Figure 2. Zero values are true zero: locations under the ice shelf where the water column are completely mixed. Last column indicates how much of each model domain does not resolve eddies.

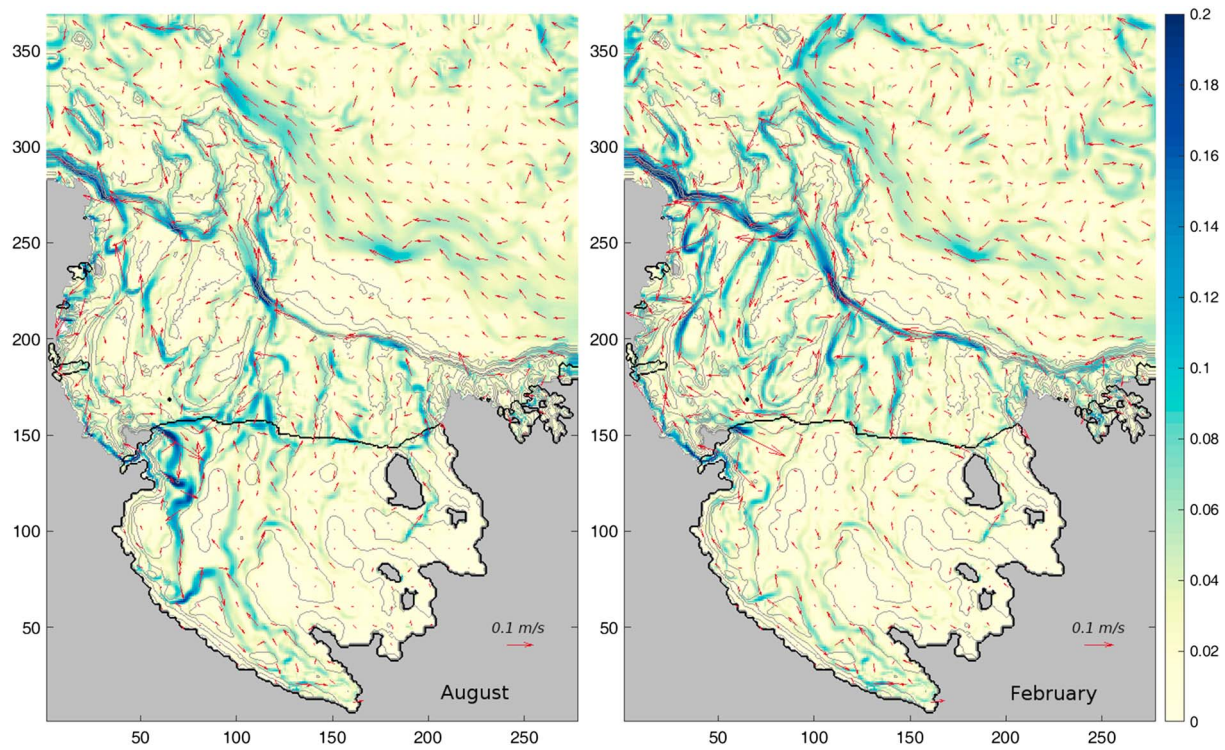

Figure 3. Monthly average barotropic velocity for August 2011 and February 2012 from simulation *5*, as color coded speed (m/s) and red arrows indicating direction. *X* and *Y* axes are model grid points (5 km per unit).

To explore the distribution of KE in each simulation, we calculated the KE components, including barotropic, baroclinic, time mean, and EKE in each simulation for the months of August and February. We restricted the analysis to locations on the continental shelf, defined by the area inshore of the 700-m isobath following the continental shelf break, including areas on the shelf deeper than 700 m while excluding the ice shelf cavity. In general, variations of the KE components over each month are driven by simulation forcing and show a similar time variability in all simulations (not shown). Monthly average KE components for August and February for the simulations show that most of the KE is barotropic, not baroclinic, with EKE and time mean components of similar magnitude (Figure 4). The monthly average of the residual KE term is less than 0.02% of the total KE for each case.

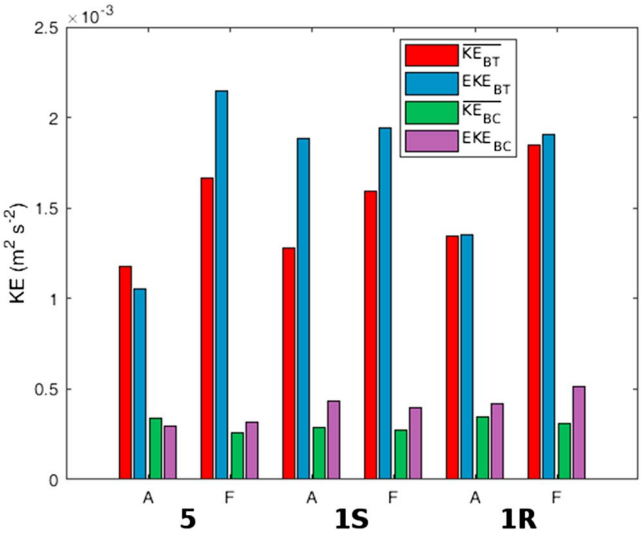

Figure 4. Month and volume average Kinetic Energy (KE) in each component (barotropic mean KE, $\overline{KE_{BT}}(x, y)$; barotropic EKE, $EKE_{BT}(x, y, t)$; baroclinic time mean KE, $\overline{KE_{BC}}(x, y, z)$; baroclinic EKE, $EKE_{BC}(x, y, z, t)$) for simulations *5*, *1R*, and *1S* for August (A) and February (F). Note that the residual KE term contributes less than 0.02% for each and is not shown.

Simulations *5* and *1S* both have higher total KE in February than in August, driven by an increase in barotropic KE. The increase may be due to higher stratification or reduced sea ice, which may allow surface winds to increase KE. Simulation *1S* has more EKE (both barotropic and baroclinic) in August than in simulation *5*, while the monthly time mean components for each are similar in magnitude. February shows the opposite effect for EKE_{BT}: there is less in simulation *1S* than in simulation *5*.

Simulation *1R* shows the same general pattern of more KE in February than in August. Compared to the smooth bathymetry case (*1S*), simulation *1R* has less KE in August, due mainly to less EKE_{BT}, and more KE in February, from an increase in $\overline{KE_{BT}}$ and EKE_{BC}. The areas where these two simulations resolve eddies are the same. Depending on the water column stratification based on season, the rougher bathymetry acts to remove barotropic eddy energy (August) or to allow more baroclinic eddy energy and more mean flow barotropic energy (February).

Table 3
Number of Eddies Tracked Over the Last Year of Simulation

Simulation	Total eddies	Eddies under ice shelf	Crossed ice shelf front
5	653	156 (24%)	65 (10%)
1S	1,559	383 (25%)	202 (13%)
1R	1,257	377 (30%)	178 (14%)

Note. Includes the total number of eddies, eddies that spent *any* time under the ice shelf, and eddies that crossed the ice shelf front. Percents are percent of the total number of eddies.

4.3. Eddy Tracking

Over the last year of each simulation, we identified and tracked coherent eddies from SSH, following the criteria listed in section 3.3 (Table 3 and Figure 5). Although simulation *5* is not eddy resolving by definition and does not capture the full eddy field, larger eddies still form. In all simulations, eddy activity is mainly restricted to the continental shelf and slope, with a large portion of eddies appearing on the inner continental shelf in front of the Ross Ice Shelf in *1S* and *1R*. The general distribution of eddies appears similar; the higher numbers of eddies in simulations *1S* and *1R* are mostly a result of higher concentrations of eddies in the same areas as they appear in simulation *5*.

The eddy tracks in Figure 5 indicate that a nonnegligible number of coherent eddies spend some time in the ice shelf cavity, with a few traveling deep under the ice shelf along the western side. For each simulation, between 24% and 30% of eddies spent some time underneath the ice shelf, with generally less than half of those crossing the ice shelf front. The diagram in Figure 5, lower right, shows how many eddies crossed the ice shelf front and in which direction. In all simulations, eddies cross the ice shelf front in both directions, despite the potential vorticity barrier caused by the ice shelf front. Recall that, in the ROMS model, this barrier is lessened due to the smoothing of the bathymetry to minimize pressure gradient errors arising from the sigma coordinate system (see section 3.1). Simulation *1R* has a sharper ice shelf front than *1S*, but the percentage of eddies crossing the ice shelf front is similar in these two simulations, suggesting that the increased steepness of the ice shelf front in *1R* does not make a significant difference for eddies that cross the ice front by following lines of constant f/H (Grosfeld et al., 1997). For each eddy tracked in each simulation, we recorded the general characteristics of that eddy, including average eddy radius over its lifetime, amplitude of the eddy in SSH, the model day the eddy formed, and the lifetime of the eddy. These statistics are shown in Figure 6 for all eddies and for the subset of eddies that spend *any* time under the ice shelf. Generally, the distributions of eddies are similar across all three simulations. Eddy radii tend to be small, with the peak of the distribution less than 20 km. However, the peak of each distribution is significantly larger than the minimum resolvable scale, indicating that eddy radii are set by characteristics of the resolved flows that determine eddy production rather than model resolution. Eddies with radii below about 10 km appear on the inner continental shelf for *1R* and *1S* and are not present in simulation *5* by definition (Figure 5). Eddy radii for eddies that travel under the ice shelf are skewed slightly smaller, which is due to their position on the inner continental shelf where a_1 is smaller.

The SSH amplitudes of the modeled eddies are small, with almost all below 4 cm difference in SSH from eddy center to outer edge. Most eddies are very short lived, remaining coherent in simulations for only a week or two. This suggests that they experience high dissipation from friction at the top (ice) and bottom boundaries, lose energy rapidly due to the prescribed horizontal diffusivity, or are modified by nonlinear interactions in the flow. Eddies tend to form in our simulations during spring and summer and less so in austral winter, consistent with the reduced ability of the model to resolve eddies, as a_1 values are smaller in winter. Observations and numerical studies on eddies at these scales have found a seasonal cycle in intensity, with a strong peak in winter months (e.g., Sasaki et al., 2014; Su et al., 2018; Yu et al., 2019). There are several potential reasons why our results show an opposite trend. One is that the model resolution is the dominant factor in determining if an eddy forms in the model and the eddy field is controlled by time-varying a_1. Another possibility is that the sea ice cover acts to reduce eddy formation in winter months by limiting the influence of the atmosphere. A third option is that, despite the similarity in horizontal scales to previous studies, the eddies here are more closely related to a_1 and are mesoscale in character, not submesoscale.

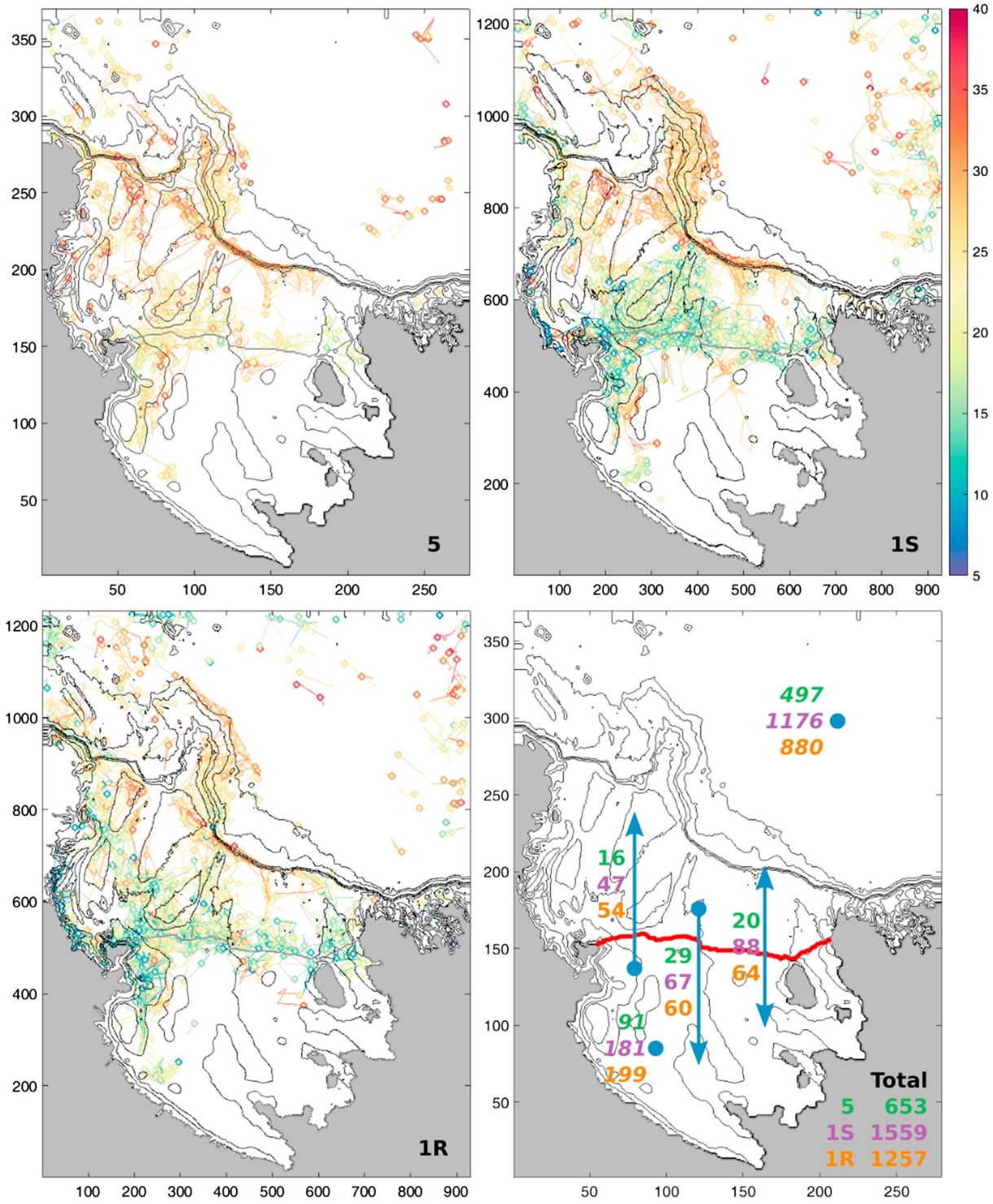

Figure 5. Maps of eddy tracks with circles indicating the starting position of the eddy during the last year of simulation for simulations *5*, *1S*, and *1R*. *X*/*Y* axes are grid points. Eddy tracks are colored by average radius (km) during the eddy lifetime. Black lines are bathymetry; gray line is ice shelf front. Bottom right panel shows, categorically, the number of eddies in each simulation (*5*, *1S*,*1R*, in order) that do or do not cross the ice shelf front. Eddies that cross multiple times are indicated by the double arrow.

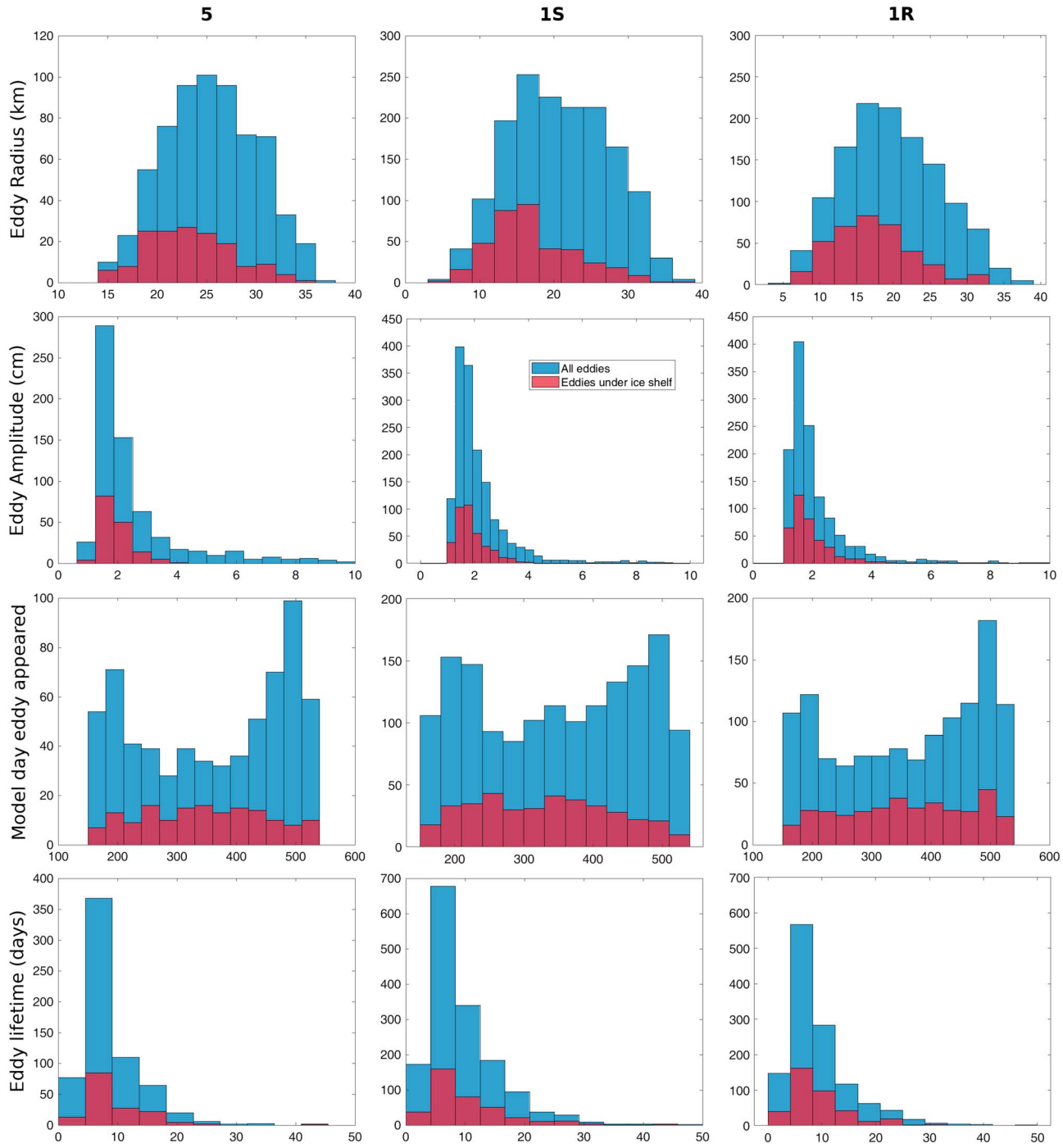

Figure 6. Histograms of eddy characteristics for the last year of simulation for *5*, *1R*, and *1S* (columns). Rows are as follows: eddy radius (km), eddy amplitude (cm), model day eddy first appeared (day 165 is 1 March; day 530 is 27 February), and eddy lifetime (days). Blue bars are all the eddies; red bars are eddies that spent any time under an ice shelf.

The relevant difference between the two is the relative magnitude of vertical and horizontal motion. In a hydrostatic model such as ROMS, we expect to model mesoscale processes that are mostly two dimensional but not correctly capture more three-dimensional submesoscale processes.

4.4. Ice Shelf Basal Melt

For each simulation, we calculated the melt over the last year of simulation and partitioned it into Mode 1 and Mode 3 (Table 4). Figure 7 shows the spatial distribution of melt from simulation *5* and which cells are

Table 4
Average Basal Melt Rate (w_b) and Area-Integrated Basal Mass (M_b) Losses Over the Last Year of Simulation

Simulation	Total w_b (cm/year)	Total M_b (GT/year)	Mode 1 M_b (GT/year)	Mode 3 M_b (GT/year)
5	21.4 ± 0.94	102.0	64.0	38.6
1S	20.1 ± 0.88	92.6	54.6	38.0
1R	22.5 ± 0.99	108.2	63.1	45.1

Note. Total melt is given as an area average (w_b, cm/year) and as a sum for the whole ice shelf (M_b, GT/year; GT is gigatons). The total melt is the sum of Mode 1 melt, Mode 3 melt, and any refreezing. The error for w_b is 4.4% of the total; see Mack et al. (2017) for a discussion of the error estimate.

identified as Mode 1, Mode 3, or no-melt cells. Results from simulations *1S* and *1R* show the same pattern. The total M_b is slightly higher than some recent observations, for example, 48 ± 34 GT/year by Rignot et al. (2013) and within the range of others, for example, 79 ± 28 GT/year by Depoorter et al. (2013). This version of ROMS does not include a parameterization for frazil ice (Galton-Fenzi et al., 2012), which may increase mass accumulation through marine ice formation and therefore decrease simulated total M_b, bringing it closer to observed values.

A quantitative estimate of whether the difference in basal melt is significant was described by Mack et al. (2017); for w_b this value is 4.4%. Using this value as an error bar for cross-simulation comparisons, simulations *1S* and *1R* are significantly different from each other. Simulation *1R* shows more total M_b than *1S*, driven by greater mass loss in both Mode 1 and Mode 3 melt. However, simulation *5* is not significantly different from either high-resolution simulation. There is no change in Mode 1 or 3 M_b related to the number of eddies in a simulation, as the values for *5* and *1S* are similar despite the large difference in the number of eddies tracked (Figure 5 and Table 3).

The lack of a significant difference between high- and low-resolution simulations indicates that it may not be necessary to use expensive high-resolution models (subkilometer scale) to obtain realistic estimates of basal melt for the Ross Ice Shelf and other Antarctic cold water ice shelves. Recall, however, that even at 1.5-km grid spacing, these simulations are not fully eddy resolving. Furthermore, higher resolution allows for a more accurate representation of the steep ice shelf front and may play a significant role in simulated Mode 3 melt even in the absence of eddies.

5. Discussion and Conclusion

The expected size of baroclinic eddies scales with the first baroclinic radius of deformation (a_1), which is a function of latitude and stratification. Previous studies have indicated that numerical ocean models with lat-

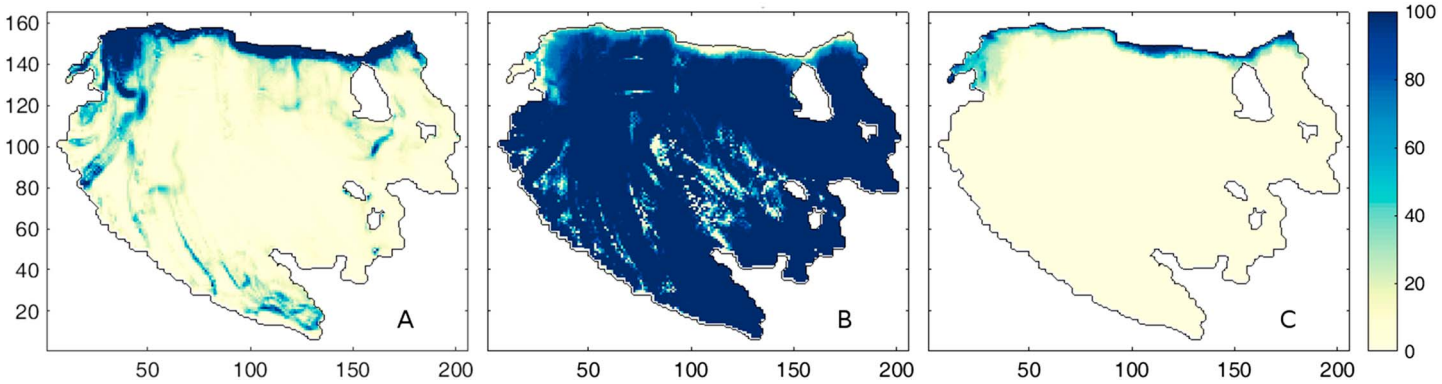

Figure 7. (a) Yearly average melt rate (w_b) from simulation *5* given in centimeter per year. (b, c) Percent of the year each cell is classified as Mode 1 (b) or Mode 3 (c) melt. Some cells are either due to freezing or no melt.

eral grid spacing of ~1–2 km adequately resolve eddies that transport heat as CDW across continental shelves of the Amundsen and Bellingshausen Seas. These CDW eddies must be resolved to generate sufficient heat flux to obtain the observed melt rates for ice shelves in that sector. This grid spacing is insufficient to resolve all scales of baroclinic variability in the weakly stratified Ross Sea continental shelf region, especially in winter when stratification is a minimum.

Simulations of the Ross Sea with grid spacings of 5 and 1.5 km do, however, produce coherent eddies identified through SSH anomalies. Decreasing the horizontal grid spacing increases the number of eddies generated in the domain, with typical eddy sizes being slightly smaller in the higher-resolution simulations. Changes in eddy generation rate are sensitive to how much topographic smoothing is applied. More eddies are observed when topography is smoother, suggesting that the associated reduction in dissipation of baroclinic energy is more important than the expected decrease in eddy generation when topographic gradients are reduced.

As the total number of eddies increases with decreasing horizontal grid spacing and smoother topography, so does the number of eddies that cross the ice shelf front in both directions. These changes in eddy frequency, size, and motion do not, however, have a significant effect on the distribution and net magnitude of ice shelf melting. Basal melting of the Ross Ice Shelf is primarily driven by inflows of Antarctic Surface Water melting thinner ice near the ice shelf front (Mode 3 melt as defined by Jacobs et al., 1992) and inflows of High Salinity Shelf Water that melt ice near the grounding line (Mode 1 melt). In our simulations, mean circulation (Figure 3) drives both melt modes regardless of eddy resolution. Unlike Mode 2 melting driven by eddies of warm subsurface water, such as CDW, Mode 1 and Mode 3 melting is not controlled by eddy processes, at least at these grid spacings. We note that the characteristics of cold water shelves that primarily melt ice shelves through Mode 1 and Mode 3, that is, a weak CDW signature and deep winter mixing, favor short-lived eddies that are small.

Further decreases of horizontal grid spacing to the subkilometer scale may shed more light on eddy effects on Mode 1 and Mode 3 basal melt. A fully eddy-resolving horizontal resolution may result in sufficient eddy activity to influence basal melt rates. That would require a significant increase in computational resources, as well as a nonhydrostatic model to resolve essential baroclinic physics driving ice shelf-ocean interactions. Even with model improvements, there may be insufficient mean KE (Figure 3) to drive significant eddy generation, with the possible exception of regions with strong mean currents, such as under the western ice shelf in winter (Figure 3, left). We speculate that even if eddies do not contribute to ice shelf basal melt, they may contribute to the transport of other water properties, such as nutrients and chemical tracers, across the ice shelf front and along sub-ice shelf pathways.

The large change in the number of eddies tracked in each simulation is not reflected in the distributions of total KE or individual components. In all three simulations, there are higher values of total KE during the more stratified summer conditions in February than in August. Grid spacing and bathymetry smoothing have small effects on which KE term is smaller or larger: finer horizontal resolution increases the amount of EKE in the winter and decreases it in the summer, while rougher bathymetry decreases barotropic EKE in winter and allows an increase of baroclinic EKE in summer. The eddies tracked here are either barotropic or have some surface expression. This restriction is imposed by the algorithm that tracks eddies by SSH. Our choice to focus on surface eddies leaves open questions about deep baroclinic eddies and how they may change between simulations and seasons.

Based on these results, we conclude that higher resolution is needed to increase understanding of eddy processes in weakly stratified Antarctic shelf seas. Resolution of 1.5 km is sufficient for ice cavities where the water column is characterized by a relatively strong thermocline, such as in the Amundsen Sea. However, this resolution does not resolve eddy processes within the Ross Ice Shelf cavity (Årthun et al., 2013). At the same time, the weak stratification that sets a small a_1 suggests that there will be less eddy activity to resolve. We anticipate that modelers of ice shelf cavities will wish to go to higher resolution for different reasons, for example, to resolve basal channels under ice shelves, which are important for determining basal melt and cavity circulation (Alley et al., 2016; Dutrieux et al., 2013; Gourmelen et al., 2017; Millgate et al., 2013). As subkilometer ice shelf cavity models are developed, we recommend analyzing these models for their ability to resolve ocean eddies and the eddy contribution to ice shelf basal melt.

Acknowledgments
This research was funded by NSF's Antarctic Research Program (ANT-0944174, ANT-0944165, and ANT-1443677), Ocean Sciences Program (OCE-1357522), and by the Future of Ice Initiative at the University of Washington. It was supported by the Turing High Performance Computing Cluster at Old Dominion University. S. M. acknowledges the support of her dissertation committee. Portions of this work appear in S. M.'s PhD thesis. The eddy tracking code and specific version of ROMS are on S. M.'s github (https://github.com/mnemoniko). Forcing files to run the simulations described are in three separate records on zenodo.org under DOIs 10.5281/zenodo.2649541, 10.5281/zenodo.2649547, and 10.5281/zenodo.2650294. We thank three anonymous reviewers for their helpful suggestions.

References

Abernathey, R., & Haller, G. (2018). Transport by lagrangian vortices in the eastern Pacific. *Journal of Physical Oceanography*, *48*(3), 667–685.

Alley, K. E., Scambos, T. A., Siegfried, M. R., & Fricker, H. A. (2016). Impacts of warm water on Antarctic ice shelf stability through basal channel formation. *Nature Geoscience*, *9*, 290–293.

Arndt, J. E., Schenke, H. W., Jakobsson, M., Nitsche, F. O., Buys, G., Goleby, B., et al. (2013). The International Bathymetric Chart of the Southern Ocean (IBCSO) version 1.0—A new bathymetric compilation covering circum-Antarctic waters. *Geophysical Research Letters*, *40*, 3111–3117. https://doi.org/10.1002/grl.50413

Årthun, Marius, Holland, P. R., Nicholls, K. W., & Feltham, D. L. (2013). Eddy-driven exchange between the open ocean and a sub-ice shelf cavity. *Journal of Physical Oceanography*, *43*(11), 2372–2387. https://doi.org/10.1175/JPO-D-13-0137.1

Beckmann, A., & Haidvogel, D. B. (1993). Numerical simulation of flow around a tall isolated seamount. Part I: Problem formulation and model accuracy. *Journal of Physical Oceanography*, *23*(8), 1736–1753. https://doi.org/10.1175/1520-0485(1993)023h1736:NSOFAAi2.0.CO;2

Budgell, W. P. (2005). Numerical simulation of ice-ocean variability in the Barents Sea region. *Ocean Dynamics*, *55*(3-4), 370–387. https://doi.org/10.1007/s10236-005-0008-3

Charney, J. G. (1947). The dynamics of long waves in a Baroclinic Westerly Current. *Journal of Meteorology*, *4*(5), 136–162. https://doi.org/10.1175/1520-0469(1947)004<0136:TDOLWI>2.0.CO;2

Charney, J. G. (1971). Geostrophic turbulence. *Journal of Atmospheric Sciences*, *28*(6), 1087–1095. https://doi.org/10.1175/1520-0469(1971)028h1087:GTi2.0.CO;2

Chelton, D. B., DeSzoeke, R. A., Schlax, M. G., El Naggar, K., & Siwertz, N. (1998). Geographical variability of the first baroclinic Rossby radius of deformation. *Journal of Physical Oceanography*, *28*(3), 433–460. https://doi.org/10.1175/1520-0485(1998)028<0433:GVOTFB>2.0.CO;2

Chelton, D. B., Schlax, M. G., Samelson, R. M., & de Szoeke, R. A. (2007). Global observations of large oceanic eddies. *Geophysical Research Letters*, *34*, L15606. https://doi.org/10.1029/2007GL030812

Chen, R., Thompson, A. F., & Flierl, G. R. (2016). Time-dependent eddy-mean energy diagrams and their application to the ocean. *Journal of Physical Oceanography*, *46*(9), 2827–2850. https://doi.org/10.1175/JPO-D-16-0012.1

Couto, N., Martinson, D. G., Kohut, J., & Schofield, O. (2017). Distribution of Upper Circumpolar Deep Water on the warming continental shelf of the West Antarctic Peninsula. *Journal of Geophysical Research: Oceans*, *119*, 5306–5315. https://doi.org/10.1002/2017JC012840

Dee, D. P., Uppala, S. M., Simmons, A. J., Berrisford, P., Poli, P., Kobayashi, S., et al. (2011). The ERA-Interim reanalysis: Configuration and performance of the data assimilation system. *Quarterly Journal of the Royal Meteorological Society*, *137*(656), 553–597. https://doi.org/10.1002/qj.828

Depoorter, M. A., Bamber, J. L., Griggs, J. A., Lenaerts, J. T. M., Ligtenberg, S. R. M., van den Broeke, M. R., & Moholdt, G. (2013). Calving fluxes and basal melt rates of Antarctic ice shelves. *Nature*, *502*(7469), 89–92. https://doi.org/10.1038/nature12567

Dinniman, M. S., Asay-Davis, X. S., Galton-Fenzi, B. K., Holland, P. R., Jenkins, A., & Timmermann, R. (2016). Modeling ice shelf/ocean interaction in Antarctica: A review. *Oceanography*, *29*(4), 144–153.

Dinniman, M. S., Klinck, J. M., & Smith, W. O. (2007). Influence of sea ice cover and icebergs on circulation and water mass formation in a numerical circulation model of the Ross Sea, Antarctica. *Journal of Geophysical Research*, *112*(C11), C11013. https://doi.org/10.1029/2006JC004036

Dinniman, M. S., Klinck, J. M., & Smith, W. O. (2011). A model study of Circumpolar Deep Water on the West Antarctic Peninsula and Ross Sea continental shelves. *Deep-Sea Research Part II: Topical Studies in Oceanography*, *58*(13-16), 1508–1523. https://doi.org/10.1016/j.dsr2.2010.11.013

Dupont, T. K., & Alley, R. B. (2005). Assessment of the importance of ice-shelf buttressing to ice-sheet flow. *Geophysical Research Letters*, *32*, L04503. https://doi.org/10.1029/2004GL022024

Dutrieux, P., De Rydt, Jan, Jenkins, A., Holland, P. R., Ha, H. K., Lee, S. H., et al. (2014). Strong sensitivity of Pine Island ice-shelf melting to climatic variability. *Science*, *343*(6167), 174–178. https://doi.org/10.1126/science.1244341

Dutrieux, P., Vaughan, D. G., Corr, H. FJ, Jenkins, A., Holland, P. R., Joughin, I., & Fleming, A. H. (2013). Pine Island glacier ice shelf melt distributed at kilometre scales. *Cryosphere*, *7*(5), 1543–1555. https://doi.org/10.5194/tc-7-1543-2013

Eady, E. T. (1949). Long waves and cyclone waves. *Tellus*, *1*(3), 33–52. https://doi.org/10.3402/tellusa.v1i3.8507

Ferrari, R., & Wunsch, C. (2009). Ocean circulation kinetic energy: Reservoirs, sources, and sinks. *Annual Review of Fluid Mechanics*, *41*(1), 253–282. https://doi.org/10.1146/annurev.fluid.40.111406.102139

Fretwell, P., Pritchard, H. D., Vaughan, D. G., Bamber, J. L., Barrand, N. E., Bell, R., et al. (2013). Bedmap2: Improved ice bed, surface and thickness datasets for Antarctica. *The Cryosphere*, *7*(1), 375–393. https://doi.org/10.5194/tc-7-375-2013

Galton-Fenzi, B. K., Hunter, J. R., Coleman, R., Marsland, S. J., & Warner, R. C. (2012). Modeling the basal melting and marine ice accretion of the Amery Ice Shelf. *Journal of Geophysical Research*, *117*, C09031. https://doi.org/10.1029/2012JC008214

Gaube, P., & McGillicuddy, D. J. (2017). The influence of Gulf Stream eddies and meanders on near-surface chlorophyll. *Deep Sea Research Part I Oceanographic Research Paper*, *122*, 1–16. https://doi.org/10.1016/j.dsr.2017.02.006

Gille, S. T., Yale, M. M., & Sandwell, D. T. (2000). Global correlation of mesoscale ocean variability with seafloor roughness from satellite altimetry. *Geophysical Research Letters*, *27*(9), 1251–1254. https://doi.org/10.1029/1999GL007003

Goldberg, D., Holland, D. M., & Schoof, C. (2009). Grounding line movement and ice shelf buttressing in marine ice sheets. *Journal of Geophysical Research*, *114*, F04026. https://doi.org/10.1029/2008JF001227

Gourmelen, N., Goldberg, D. N., Snow, K., Henley, S. F., Bingham, R. G., Kimura, S., et al. (2017). Channelized melting drives thinning under a rapidly melting antarctic ice shelf. *Geophysical Research Letters*, *44*, 9796–9804. https://doi.org/10.1002/2017GL074929

Graham, J. A., Dinniman, M. S., & Klinck, J. M. (2016). Impact of model resolution for on-shelf heat transport along the West Antarctic Peninsula. *Journal of Geophysical Research: Oceans*, *121*, 7880–7897. https://doi.org/10.1002/2016JC011875

Grosfeld, K., Gerdes, R., & Determann, J. (1997). Thermohaline circulation and interaction between ice shelf cavities and the adjacent open ocean. *Journal of Geophysical Research*, *102*(C7), 15,595–15,610. https://doi.org/10.1029/97JC00891

Haidvogel, D. B., Arango, H., Budgell, W. P., Cornuelle, B. D., Curchitser, E., Di Lorenzo, E., et al. (2008). Ocean forecasting in terrain-following coordinates: Formulation and skill assessment of the Regional Ocean Modeling System. *Journal of Computational Physics*, *227*(7), 3595–3624. https://doi.org/10.1016/j.jcp.2007.06.016

Hallberg, R. (2013). Using a resolution function to regulate parameterizations of oceanic mesoscale eddy effects. *Ocean Modelling*, *72*, 92–103. https://doi.org/10.1016/j.ocemod.2013.08.007

Haney, R. L. (1991). On the pressure gradient force over steep topography in sigma coordinate ocean models. *Journal of Physical Oceanography*, *21*(4), 610–619. https://doi.org/10.1175/1520-0485(1991)021h0610:OTPGFOi2.0.CO;2

Hattermann, T., Smedsrud, L. H., Nøst, O. A., Lilly, J. M., & Galton-Fenzi, B. K. (2014). Eddy-resolving simulations of the Fimbul Ice Shelf cavity circulation: Basal melting and exchange with open ocean. *Ocean Modelling*, *82*, 28–44. https://doi.org/10.1016/j.ocemod.2014.07.004

Holland, D. M., & Jenkins, A. (1999). Modeling thermodynamic ice-ocean interactions at the base of an ice shelf. *Journal of Physical Oceanography*, *29*(8), 1787–1800. https://doi.org/10.1175/1520-0485(1999)029h1787:MTIOIAi2.0.CO;2

Isern-Fontanet, J., García-Ladona, E., & Font, J. (2003). Identification of marine eddies from altimetric maps. *Journal of Atmospheric and Oceanic Technology*, *20*(5), 772–778. https://doi.org/10.1175/1520-0426(2003)20h772:IOMEFAi2.0.CO;2

Jacobs, S. S., Helmer, H. H., Doake, C. S. M., Jenkins, A., & Frolich, R. M. (1992). Melting of ice shelves and the mass balance of Antarctica. *Journal of Glaciology*, *38*(130), 375–387. https://doi.org/10.3189/S0022143000002252

Jacobs, S. S., Jenkins, A., Giulivi, C. F., & Dutrieux, P. (2011). Stronger ocean circulation and increased melting under Pine Island Glacier ice shelf. *Nature Geoscience*, *4*(8), 519–523. https://doi.org/10.1038/ngeo1188

Jendersie, S., Williams, M. J. M., Langhorne, P. J., & Robertson, R. (2018). The density-driven winter intensification of the Ross Sea circulation. *Journal of Geophysical Research: Oceans*, *123*, 7702–7724. https://doi.org/10.1029/2018JC013965

Joughin, I., & Padman, L. (2003). Melting and freezing beneath Filchner-Ronne Ice Shelf, Antarctica. *Geophysical Research Letters*, *30*(9), 1477. https://doi.org/10.1029/2003GL016941

Large, W. G., McWilliams, J. C., & Doney, S. C. (1994). Oceanic vertical mixing: A review and a model with a nonlocal boundary layer parameterization. *Reviews of Geophysics*, *32*(4), 363. https://doi.org/10.1029/94RG01872

Li, Y., McGillicuddy, D. J., Dinniman, M. S., & Klinck, J. M. (2017). Processes influencing formation of low-salinity high-biomass lenses near the edge of the Ross Ice Shelf. *Journal of Marine Systems*, *166*, 108–119. https://doi.org/10.1016/j.jmarsys.2016.07.002

Liu, C., Wang, Z., Cheng, C., Xia, R., Li, B., & Xie, Z. (2017). Modeling modified Circumpolar Deep Water intrusions onto the Prydz Bay continental shelf, East Antarctica. *Journal of Geophysical Research: Oceans*, *122*, 5198–5217. https://doi.org/10.1002/2016JC012336

MacCready, P., & Giddings, S. N. (2016). The mechanical energy budget of a regional ocean model. *Journal of Physical Oceanography*, *46*(9), 2719–2733. https://doi.org/10.1175/JPO-D-16-0086.1

Mack, S. L., Dinniman, M. S., McGillicuddy, D. J., Sedwick, P. N., & Klinck, J. M. (2017). Dissolved iron transport pathways in the Ross Sea: Influence of tides and horizontal resolution in a regional ocean model. *Journal of Marine Systems*, *166*, 73–86. https://doi.org/10.1016/j.jmarsys.2016.10.008

Marques, G. M., & Özgökmen, T. M. (2014). On modeling turbulent exchange in buoyancy-driven fronts. *Ocean Modelling*, *83*, 43–62. https://doi.org/10.1016/j.ocemod.2014.08.006

Marshall, J., Hill, C., Perelman, L., & Adcroft, A. (1997). Hydrostatic, quasi-hydrostatic, and nonhydrostatic ocean modeling. *Journal of Geophysical Research*, *102*(C3), 5733–5752. https://doi.org/10.1029/96JC02776

Martinson, D. G., & McKee, D. C. (2012). Transport of warm upper circumpolar deep water onto the Western Antarctic Peninsula Continental Shelf. *Ocean Science*, *8*(4), 433–442. https://doi.org/10.5194/os-8-433-2012

McDougall, T. J., & Barker, P. M. (2011). Getting started with TEOS-10 and the Gibbs Seawater (GSW) Oceanographic Toolbox. *SCOR/IAPSO WG*, *27*, 1–28.

McGillicuddy, D. J., Sedwick, P. N., Dinniman, M. S., Arrigo, K. R., Bibby, T. S., Greenan, B. J. W., et al. (2015). Iron supply and demand in an Antarctic shelf ecosystem. *Geophysical Research Letters*, *42*, 8088–8097. https://doi.org/10.1002/2015GL065727

McWilliams, J. C. (2008). The nature and consequences of oceanic eddies, *Ocean modeling in an eddying regime* (pp. 5–15). Washington, D. C.: AGU.

Mercer, J. H. (1978). West Antarctic Ice Sheet and CO_2 greenhouse effect: A threat of disaster.*Nature*, *271*(5643), 321–325. https://doi.org/10.1038/271321a0

Millgate, T., Holland, P. R., Jenkins, A., & Johnson, H. L. (2013). The effect of basal channels on oceanic ice-shelf melting. *Journal of Geophysical Research: Oceans*, *118*, 6951–6964. https://doi.org/10.1002/2013JC009402

Moffat, C., Owens, B., & Beardsley, R. C. (2009). On the characteristics of Circumpolar Deep Water intrusions to the west Antarctic Peninsula Continental Shelf. *Journal of Geophysical Research*, *114*, C05017. https://doi.org/10.1029/2008JC004955

Nakayama, Y., Timmermann, R., Schröder, M., & Hellmer, H. (2014). On the difficulty of modeling Circumpolar Deep Water intrusions onto the Amundsen Sea continental shelf. *Ocean Modelling*, *84*, 26–34. https://doi.org/10.1016/j.ocemod.2014.09.007

Nowicki, S., Bindschadler, R. A., AbeâĂŘOuchi, A., Aschwanden, A., Bueler, E., Choi, H., et al. (2013). Insights into spatial sensitivities of ice mass response to environmental change from the SeaRISE ice sheet modeling project I: Antarctica. *Journal of Geophysical Research: Earth Surface*, *118*, 1002–1024. https://doi.org/10.1002/jgrf.20081

Pritchard, H. D., Ligtenberg, S. R. M., Fricker, H. A., Vaughan, D. G., van den Broeke, M. R., & Padman, L. (2012). Antarctic ice-sheet loss driven by basal melting of ice shelves. *Nature*, *484*(7395), 502–5. https://doi.org/10.1038/nature10968

Rignot, E., Jacobs, S., Mouginot, J., & Scheuchl, B. (2013). Ice-shelf melting around Antarctica. *Science*, *341*(6143), 266–270. https://doi.org/10.1126/science.1235798

Sasaki, H., Klein, P., Qiu, B., & Sasai, Y. (2014). Impact of oceanic-scale interactions on the seasonal modulation of ocean dynamics by the atmosphere. *Nature communications*, *5*, 5636.

Scott, R. B., & Wang, F. (2005). Direct evidence of an oceanic inverse kinetic energy cascade from satellite altimetry. *Journal of Physical Oceanography*, *35*(9), 1650–1666.

Shchepetkin, A. F., & McWilliams, J. C. (2005). The regional oceanic modeling system (ROMS): A split-explicit, free-surface, topography-following-coordinate oceanic model. *Ocean Modelling*, *9*(4), 347–404. https://doi.org/10.1016/j.ocemod.2004.08.002

Shchepetkin, A. F., & McWilliams, J. C. (2009). Correction and commentary for "Ocean forecasting in terrain-following coordinates: Formulation and skill assessment of the regional ocean modeling system" by Haidvogel et al., J. Comp. Phys. 227, pp. 3595-3624. *Journal of Computational Physics*, *228*(24), 8985–9000. https://doi.org/10.1016/j.jcp.2009.09.002

Smith, K. S., & Vallis, G. K. (2001). The scales and equilibration of midocean eddies: Freely evolving flow. *Journal of Physical Oceanography*, *31*, 554–571. https://doi.org/10.1175/1520-0485(2002)032h1699:TSAEOMi2.0.CO;2

Smith, K. S., & Vallis, G. K. (2002). The scales and equilibration of midocean eddies: Forced-dissipative flow. *Journal of Physical Oceanography*, *32*(6), 1699–1720. https://doi.org/10.1175/1520-0485(2002)032h1699:TSAEOMi2.0.CO;2

Song, Y., & Haidvogel, D. (1994). A semi-implicit ocean circulation model using a generalized topography-following coordinate system. *Journal of Computational Physics*, *115*(1), 228–244. https://doi.org/10.1006/jcph.1994.1189

St-Laurent, P., Klinck, J. M., & Dinniman, M. S. (2013). On the role of coastal troughs in the circulation of warm Circumpolar Deep Water on Antarctic shelves. *Journal of Physical Oceanography*, *43*(1), 51–64. https://doi.org/10.1175/JPO-D-11-0237.1

St-Laurent, P., Klinck, J. M., & Dinniman, M. S. (2015). Impact of local winter cooling on the melt of Pine Island Glacier, Antarctica. *Journal of Geophysical Research: Oceans*, *120*, 6718–6732. https://doi.org/10.1002/2015JC010709

Stammer, D. (1998). On eddy characteristics, eddy transports, and mean flow properties. *Journal of Physical Oceanography*, *28*(4), 727–739. https://doi.org/10.1175/1520-0485(1998)028h0727:OECETAi2.0.CO;2

Stewart, A. L., Klocker, A., & Menemenlis, D. (2018). Circum-Antarctic shoreward heat transport derived from an eddy- and tide-resolving simulation. *Geophysical Research Letters*, *45*, 834–845. https://doi.org/10.1002/2017GL075677

Stewart, A. L., & Thompson, A. F. (2015). Eddy-mediated transport of warm Circumpolar Deep Water across the Antarctic Shelf Break. *Geophysical Research Letters*, *42*, 432–440. https://doi.org/10.1002/2014GL062281

Su, Z., Ingersoll, A. P., Stewart, A. L., & Thompson, A. F. (2016). Ocean convective available potential energy. Part I: Concept and calculation. *Journal of Physical Oceanography*, *46*(4), 1081–1096.

Su, Z., Stewart, A. L., & Thompson, A. F. (2014). An idealized model of Weddell gyre export variability. *Journal of Physical Oceanography*, *44*(6), 1671–1688.

Su, Z., Wang, J., Klein, P., Thompson, A. F., & Menemenlis, D. (2018). Ocean submesoscales as a key component of the global heat budget. *Nature communications*, *9*(1), 775.

Vallis, G. K. (2006). *Atmospheric and oceanic fluid dynamics*. Cambridge: Cambridge University Press. https://doi.org/10.1002/qj.186

Webb, D. J., Coward, A. C., De Cuevas, B. A., & Gwilliam, C. S. (1997). A multiprocessor ocean general circulation model using message passing. *Journal of Atmospheric and Oceanic Technology*, *14*(1), 175–183. https://doi.org/10.1175/1520-0426(1997)014h0175:AMOGCMi2.0.CO;2

Yu, X., Naveira Garabato, A. C., Martin, A. P., Buckingham, C. E., Brannigan, L., & Su, Z. (2019). An annual cycle of submesoscale vertical flow and restratification in the upper ocean. *Journal of Physical Oceanography*, *49*(6), 1439–1461.